

Final Draft
of the original manuscript:

Gabrisch, H.; Lorenz, U.; Pyczak, F.; Rackel, M.; Stark, A.:

**Morphology and stability of orthorhombic and hexagonal phases
in a lamellar Gamma-Ti-42Al-8.5Nb alloy-A transmission electron
microscopy study**

In: Acta Materialia (2017) Elsevier

DOI: 10.1016/j.actamat.2017.05.067

MORPHOLOGY AND STABILITY OF ORTHORHOMBIC AND HEXAGONAL PHASES IN A LAMELLAR γ -Ti-42Al-8.5Nb ALLOY- A TRANSMISSION ELECTRON MICROSCOPY STUDY

Heike Gabrisch^{*}, Uwe Lorenz, Florian Pyczak, Marcus Rackel, Andreas Stark

Institute of Materials Research, Helmholtz-Zentrum Geesthacht

Max Planck-Str.1, 21502 Geesthacht, Germany

Abstract

Intermetallic titanium aluminides are often alloyed with niobium to improve oxidation resistance and mechanical properties. Depending on the overall alloy composition and on the solubility of the present phases for niobium, new phases may be introduced in the alloys' microstructure upon niobium addition. Here we describe the microstructure of the alloy Ti-42Al-8.5Nb produced by powder metallurgy after annealing at 550 °C and 650 °C. We identify the orthorhombic O-phase within α_2 laths of lamellar ($\alpha_2\gamma$) colonies by single crystal electron diffraction and high-resolution imaging. Domains of O-phase variants and α_2 phase form columnar crystallites in α_2 (0001) planes having low indexed α_2 {11-20} and {1-100} interface planes. The nm-sized domains are rotated with respect to each other resulting in elastic strains across the domain boundaries. No elemental segregation of Nb was detected in α_2 /O-phase lamellae.

key words: Titanium aluminides, O-phase, Solid state transformation, in-situ transmission electron microscopy, HRTEM

*corresponding author, e-mail address: heike.gabrisch@hzg.de

1. INTRODUCTION

Intermetallic γ -TiAl alloys are an important class of light-weight materials with high specific strength and good creep properties up to high temperatures that make them designated candidates for applications in the air craft industry [1-4]. Depending on composition and processing route the alloys form the major ordered phases β_o (cubic, B2), α_2 (hexagonal, DO_{19}) and γ (tetragonal, $L1_0$), whereby the so-called γ -TiAl alloys consist mainly of the ordered hexagonal and tetragonal phases α_2 and γ [1-3, 5].

The requirements for practical applications include high yield strength at service temperature, acceptable room-temperature ductility and oxidation resistance. Early on during the development of γ -TiAl alloys it was found that alloying with niobium enhances oxidation resistance as well as creep strength and ductility [6-9].

In alloys containing high amounts of niobium, the orthorhombic phase B19 was detected within the alloys' microstructures that is thought to be responsible for improved room temperature ductility [10-13]. Only little detail exists on the nature of this orthorhombic phase or on its distribution within the microstructure of intermetallic γ -TiAl alloys. On the other hand, the orthorhombic O-phase has been known to exist in α_2 based Ti-aluminides since the late 1980ies [14, 15]. The crystallography and morphology of the O-phase has been described comprehensively for α_2 based TiAl alloys in the composition range Ti-(12-31)Al-(12.5-37)Nb (all compositions are given in at.-% throughout this text) [14, 16-23]. Recently we identified the orthorhombic O-phase for the first time in a γ -TiAl based alloy of the composition Ti-42Al8.5Nb [24]. This finding is new regarding the alloy's relatively low Nb content in comparison to that of the stoichiometric O-phase Ti-25Al-25Nb. Single crystal electron diffraction and in-situ heating high-energy x-ray diffraction (HEXRD) confirmed that the new phase forms out of the α_2 phase and that it is the orthorhombic O-phase.

Major differences between the O-phase in the present alloy and the O-phase reported in literature lie in the low Nb content of the present alloy and in the phase morphology of the different alloys. The present alloy consists of lamellar ($\alpha_2 + \gamma$) colonies where the phase transformation from α_2 to orthorhombic phase takes place in a constraint environment. For comparison, the transformations described in literature occur within globular grains of the phases α_2 or β_0 [17, 19-21].

The purpose of this paper is to describe the spatial arrangement of the phases involved in the α_2 to O-phase transformation within lamellar colonies of the alloy Ti-42Al-8.5Nb. The results of TEM investigations show that the transformation of the hexagonal α_2 phase yields three crystallographic equivalent orthorhombic domains that form a faceted arrangement within the parent α_2 laths. The former α_2 lamellae have transformed to compound α_2 /O-phase lamellae. No Nb enriched regions were detected in the parent or product phase by the methods used. We show how the strain contrast observed in edge-on projections of lamellar colonies described in [10] is related to the domain formation described in [20]. Finally, we demonstrate that internal strains between the phases α_2 and γ in lamellar colonies play a role in the stability of the observed O-phase.

2. EXPERIMENTAL

The alloy Ti-42Al-8.5Nb was produced in house following a powder metallurgical route. Starting from pure elements buttons were molten by plasma arc melting [25]. The buttons were re-molten four times to ensure chemical homogeneity and were cast into rods. From the rods powder was produced by the EIGA technique (Electrode Induction Melting Gas Atomization). Powder particles with diameters 45-180 μm were filled into titanium cans and were compacted by hot-isostatic pressing (HIP) in Ar at 1250 $^\circ\text{C}$ under 200 MPa for 2 h. From the HIPed compacts specimens were prepared for heat treatments. The specimens were annealed in air either at 650 $^\circ\text{C}$ for 2 hours or at 550 $^\circ\text{C}$ between 1 and 4 weeks, followed by furnace cooling.

A button of the composition Ti-30Al5Nb was produced from pure elements by arc melting under argon atmosphere. It was used as standard to determine k-factors for EDS measurements in the TEM. The Al concentration of 30 at.% was chosen to ensure a single phase alloy constitution. The button was remolten > 10 times to ensure homogeneity. The composition of the standard was verified by weighing the material before and after arc melting and by EDS measurements in a scanning electron microscope. The weight loss during arc melting was -0.043 g of 31.9924 g or 0.13 %.

For Transmission Electron Microscopy 500 μm thick slices were cut of the annealed specimens and discs of 2.3 mm diameter were drilled out of these slices. The discs were ground manually to about 120 μm thickness followed by polishing in a twin jet polisher, Fischione Model 120, with a solution of 18 ml perchloric acid in 430 ml methanol and 250 ml 2-buthanol at -39 °C (flow rate 1-2). The TEM specimens were investigated by diffraction contrast in a Philips CM 200 TEM operated at 200 kV. Some TEM foils were investigated by in-situ heating in the CM 200 using a Gatan double tilt heating holder. High-resolution imaging, EDS analysis and HAADF-STEM imaging were performed in a Cs image corrected FEI Titan 80-300 TEM operated at 300 kV. The high resolution images were recorded at defocus values of 25 nm (planar view) and 5 nm (edge-one projections) and were compared to images simulated under variation of thickness and defocus at a Cs value of 0.01 mm. For some high resolution investigations Cs values were measured with the image corrector before and after the TEM session. Typical values were 300 nm -700nm at the beginning of a session and > 1 μm at the end (up to 7 μm).

EDS spectra were recorded with an EDAX detector (TOPS-30 (OST)) under tilt angles of 0, 10-12°, and 19-20° towards the detector. For quantification k-factors for Al-K and Nb-L lines with respect to Ti-K were determined from the standard Ti-30Al-5Nb using the software program TIA. In the spectra of the standard the integrated intensity in the smallest peak used for evaluation (Nb-L) was $28 \cdot 10^3$ counts on average. Mean values for k-factors were obtained from 64 measurements and the standard file that best represents the mean values of the k-factors for Al-K and Nb-L was chosen for evaluation of the alloy's

spectra. Based on 64 measurements the average k-factor for Al is 0.750 with a margin of error of 0.006 (0.8%) and the average k-factor for Nb is 2.487 with a margin of error of 0.042 (1.7%) for a 95% confidence interval. The k-factors of the file chosen as standard file are 0.747 (-0.0034 of mean) and 2.482 (=0.0051 of mean) – both within the margin of error.

The composition of α_2 and γ lamellae in the alloy Ti-42Al-8.5Nb were investigated in edge-on orientations of lamellar colonies avoiding exact zone axis orientations. Point measurements in STEM or TEM mode at spot size 6-7 were performed on α_2 and γ lamellae in specimens in the HIPed state and after annealing at 550°C for 672h (4 weeks). The average number of counts in the integrated intensities of the evaluated peaks were 32,500 for Al-K, 51,000 for Ti-K and 8500 for Nb-L.

Experimental high-resolution images and diffraction patterns were compared to simulations generated with the software package JEMS. High-resolution EFTEM imaging and HAADF STEM imaging was performed using the FEI Titan G3 50-300 PICO at the EC-R in the research facility Jülich [26].

For the simulations we modified the unit cells of α_2 , B19 and the O-phase to reflect the experimentally measured composition of α_2 lamellae (roughly approximated as Ti-40Al-10Nb). In the α_2 unit cell (P 6 3/m m c, space group 194) Al occupies the 2d Wyckoff position and surplus Al is placed onto the 6h site. Ti and Nb occupy the 6h site based on the preference of Nb to share Ti sites [27]. In the orthorhombic O-phase (C m c m, space group 63) Al and Nb separate into predominantly Al (4c1) and Nb (4c2) sites [21]. For comparison to previous studies simulations of the orthorhombic phase B19 were included. In the B19 phase (P m m a, space group 51) Nb prefers to share sites with Al, therefore Ti is placed onto the Wyckoff position 2e and Nb/ Al occupy the 2f site [21]. Details of the unit cells used are listed in the [appendix](#).

The orientation relationship between the hexagonal α_2 and the two orthorhombic phases B19 and O-phase is : α_2 (0001) // B19 (100) // O-phase (001) and α_2 [11-20]- // B19 [0-10] // O-phase [100] [14,

28]. The α_2 $\langle 10\text{-}10 \rangle$ zone axis was chosen for investigations in edge-on projections because the often referenced $\langle 11\text{-}20 \rangle$ type zone axis is not well suited to distinguish between α_2 , B19 and O-phase. Simulations show that in $\langle 11\text{-}20 \rangle$ orientation the diffraction patterns of the three phases superimpose and the contrast behavior in high-resolution images is very similar when the experimental composition Ti-42Al-8.5Nb is considered [29]. The three $\langle 10\text{-}10 \rangle$ zone axis of the hexagonal α_2 phase correspond to two zone axis types in the orthorhombic lattice due to the lower symmetry of the orthorhombic system. These are the directions $[010]$ and $\langle 310 \rangle$ in O-phase indexing and the directions $[001]$ and $\langle 031 \rangle$ when indexed in the B19 system.

For the ease of comparison directions and planes are labeled with respect to the α_2 phase even when other phases are present. Unless noted otherwise the results for the two annealing temperatures 650 °C and 550 °C are discussed together since no fundamental differences with respect to the nature of phases present were detected.

3. RESULTS AND DISCUSSION

3.1. Overview

The alloy's microstructure consists of lamellar ($\alpha_2 + \gamma$) colonies with an average grain size of 20 - 150 μm . At grain boundaries and triple-junctions small amounts of α_2 , ω_0 and γ phases are observed. An example of the microstructure is given by the SEM image in [Fig. 1a](#). The orientation relationship between the phases inside ($\alpha_2 + \gamma$) colonies is: $(0001)_{\alpha_2} // \{111\}_{\gamma}$; $\langle 11\text{-}20 \rangle_{\alpha_2} // \langle 1\text{-}10 \rangle_{\gamma}$ as described by Blackburn [30]. In this description the tetragonal γ -phase is described in pseudo-cubic settings, where $(001)_{\text{tetra}} // (001)_{\text{cubic}}$ and $[100]_{\text{tetra}} // [110]_{\text{cubic}}$. The interface between the two phases is planar and oriented parallel to α_2 (0001) . As a result, TEM observations either provide an unobstructed view of the α_2 / γ interface (edge-on projections) or projections of the α_2 basal plane (planar view). [Fig. 1b](#) shows a schematic representation of the geometry of phases and interfaces in the lamellar colonies.

The composition of α_2 lamellae was measured as Ti-37Al-9 Nb in the HIPed state and after annealing at 550°C for 4 weeks. The corresponding composition for γ lamellae was Ti-48Al-8Nb. Detailed statistical results are given in table 1. The uncertainty of the measurements is estimated as the sum of errors in the determination of the k-factors plus the standard deviations of the measurements in table 1. This gives a relative error of 3% for Al-concentrations and of 5% for Nb concentrations, which translates into a composition range of 36.5-38.5 at.-% of Al and 8.5 – 9.5 at.-% of Nb in α_2 phase.

3.2 Edge-on projections

In **Fig. 2a** a bright field image of a lamellar ($\alpha_2+\gamma$) colony is shown in α_2 [10-10] orientation together with the corresponding diffraction pattern. The widths of α_2 and γ lamellae vary strongly between different lamellae and in different colonies. For example, in **Fig. 2** values between 34 nm and 172 nm are measured, but smaller and larger values are observed in other colonies. The contrast within the α_2 lamellae oscillates in the form of stripes that are oriented perpendicular to the α_2 / γ interface. In the diffraction pattern in **Fig. 2c** new reflections are observed that are not α_2 reflections. These lie halfway between α_2 reflections of the general notation $hh-2hl$ with $l=2$ and indicate a reduction in symmetry. The intensities observed at α_2 {001} positions are caused by double diffraction. Comparison between the experimental diffraction pattern in **Fig. 2c** and simulated diffraction patterns in **Fig. 3** shows that solely the O-phase has additional intensities at these positions (**Fig. 3c**). The diffraction patterns in the zone axis orientations B-19-[001] and O-phase-[010] are identical to that of α_2 -[10-10] and are not shown in **Fig. 3**. In **Fig. 2b** the specimen region shown in **2a.**) is imaged in dark field condition using the -261 reflection of the O-phase. It can be seen that the α_2 /O-phase laths shine bright, which demonstrates that the O-phase is located inside α_2 lamellae.

The reflections in **Fig. 2c** show streaking perpendicular to the α_2 [0001] direction. This is observed in the diffraction patterns of all annealed specimens whereby the effect is more pronounced in specimens

that were long-term-annealed at 550 °C than in those annealed at 650 °C. An illustration is given in the diffraction pattern in **Fig. 2d** that has been taken after annealing at 550 °C for 3 weeks.

In **Fig. 4** a high-resolution image shows part of a α_2 /O-phase lamella together with the neighboring γ phase. In the α_2 lamella stripes of good image resolution alternate with regions where the lattice is tilted out of orientation. The atomically resolved stripes are about 10 nm wide and are oriented perpendicular to the α_2/γ interface, comparable to the contrast modulation at lower magnification in **Fig. 2**. In **Figs. 4b** and **4c** sections of two parallel stripes, labeled b. and c., are magnified and are shown together with their Fast Fourier Transforms (FFT). In **Fig. 4b** the contrast of neighboring rows of atoms alternates between bright and dark, whereas in **Fig. 4c** all atoms have even brightness. In the corresponding FFT in **Fig. 4b** intensity is observed at the position of the $\{001\}$ long-range order "reflection" of O-phase but not in the FFT shown in **Fig. 4c**.

The images in in **Figs. 4b, c** are compared to the simulations in **Fig. 3** that were calculated for a specimen thickness of 10nm and 5 nm defocus. Tables showing image simulations for variation of defocus and thickness are given as additional material. There it can be seen that the images in **Fig. 3** are reproduced in the thickness range between 6 and 16 nm. A comparison of **Fig. 4b** to **Fig. 3** shows that image contrast and diffractogram are both in agreement with O-phase in $[310]$ orientation. For α_2 - $[10-10]$ the image contrast is identical to that of **Fig. 4b**, but the FFT does not match (no extra diffractions). B19- $[001]$ and O-phase- $[010]$ are identical to α_2 - $[10-10]$ in image and diffraction and are not shown in **Fig. 4**. For the image in **Fig. 4c** no clear identification is possible. Here the image corresponds to the Bloch wave image of B19- $[031]$ or to disordered α phase whereas the FFT matches either ordered α_2 , B19- $[001]$ or O-phase- $[010]$.

3.3 Planar view of α_2 basal plane.

An example of a lamellar colony imaged in α_2 -[0001] orientation is shown in Fig.5 together with the corresponding diffraction pattern. A striking feature in this projection is the appearance of differently oriented facets within α_2 laths that have rectangular and rhomboid shape (Fig. 5a). In the diffraction pattern, the diffracted intensities spread over an angular range of 3-7° around the positions of fundamental α_2 -{10-10} reflections (Fig 5b). Additionally, the reflections are split along the radius, indicating the presence of two sets of planes with different d-spacings (difference $\approx < 0.5 \text{ \AA}$). Both, the angular rotation and the radial split are stronger after annealing at 550 °C than after annealing at 650 °C. The simulated diffraction patterns parallel to the α_2 [0001] direction for the phases α_2 , B19 and O-phase are shown in Figs 5c-e. The diffraction patterns partly superimpose which makes a clear distinction difficult should multiple phases co-exist. Compared to the hexagonal α_2 phase the orthorhombic phases have either an identical number of reflections (O-phase) or fewer reflections (B19). The angles between fundamental reflections α_2 {1-100} (marked in Fig. 5c) are 60° in the hexagonal symmetry and become larger with increasing orthorhombic distortion, for example 65° are calculated in Fig 5e. This means that the radially distributed intensity in experimental diffraction patterns could either be the result of crystals that are rotated around the α_2 -[0001] axis with respect to each other, or of the orthorhombic distortion, or both.

In Fig. 6 a section of a faceted α_2 lath is enlarged to illustrate the orientations of the facets' interfaces. The interfaces are parallel sets of {11-20} and {1-100} type planes, e.g. the (-2110) and (0-110) interface planes define a rectangular shape or (-2110) and (-1100) define a rhomboid shape. The size of the facets varies largely within one lamella and between different lamellae in the same specimen. For example, facet sizes between 3 nm x 5 nm and 140 nm x 28 nm are measured in Fig. 6.

In order to investigate whether the faceting is accompanied by elemental segregation of Nb or other elements HAADF-STEM images were recorded of the same specimen region using different camera-lengths. In **Fig 7.a**, taken at a camera length of 300 mm (predominantly diffraction contrast), strongly shaded dark and bright facets are clearly visible. For comparison, in **Fig 7.b**, imaged with a camera length of 100 mm (predominantly z contrast), the image contrast is uniform across the entire image except for smaller details, which appear within the facets.

In experimental high-resolution images of α_2 lamellae, atomically resolved regions of the lattice are seen next to regions where the lattice is tilted out of zone axis orientation. Within the resolved regions of the lattice, different ordering behavior is observed as illustrated in **Fig 8**. In the lower left part of **Fig. 8** bright atom columns form a hexagonal patterns of six-fold symmetry. In the upper right part rows of alternating dark and bright contrast are observed parallel to the α_2 - $\langle 10\text{-}10 \rangle$ directions forming a pattern of two-fold symmetry. The interface between different regions is not atomically flat. Elastic strain between the two regions is visible from bending of lattice planes across the image, see arrow in **Fig. 8**.

Simulated high-resolution images of the hexagonal α_2 and the orthorhombic phases B19 and O-phase are shown in **Fig. 9** for a specimen thickness of 10 nm and a defocus value of 25nm. Tables showing image simulations for variation of defocus and thickness values are given as additional material. There it can be seen that the observed images are reproduced in the thickness range between 8 and 16 nm. The simulated images in **Fig. 9** seem to match the experiment, however a clear distinction between hexagonal and orthorhombic phases requires further simulations taking into account crystal tilt and strain that are out of the scope of this paper. A better proof for the presence of an orthorhombic phase is obtained by atomic resolution STEM imaging in **Fig. 10**.

In **Fig 10** a high resolution HAADF-STEM image is shown that directly illustrates the orthorhombic distortion of the lattice. In the center of the image a small region with hexagonal symmetry is encircled.

Away from the center, different regions of the lattice are enlarged. These are regions where the atomic positions deviate from the hexagonal symmetry. The new positions of the atom columns are shifted along the three α_2 $\langle 1-100 \rangle$ directions as indicated by the arrows attached to the enlarged sections of the image. Each direction of displacement forms one variant of an orthorhombic phase, so that altogether three orthorhombic domains and one hexagonal domain are shown in [Fig. 10](#).

3.4 In-situ heating

In situ heating experiments were performed with the goal to directly observe changes in facet size with annealing temperature and with annealing time. In the course of the experiment, the facets seen in [0001] projection at room temperature in [Fig. 11b](#) dissolve at approximately 600 °C. At the same time, the strain contrast in $\langle 10-10 \rangle$ projection and the long range order reflections of the O-phase that are visible at room temperature in [Fig. 11a](#) disappear. The new phase constitution is stable during cooling to room temperature and subsequent re-heating as illustrated in [Figs 11c, d](#), taken after cooling from 600°C to room temperature. In both images, the α_2 lamellae show a smooth contrast. The diffraction pattern in [Fig. 11c](#) can be indexed solely by α_2 phase and shows no streaking. In the diffraction pattern in [Fig. 11d](#) the splitting of diffractions according to the presence of two sets of lattice planes and the radial distribution of diffracted intensities are no longer observed.

4. DISCUSSION

The experimental observations can be summarized as follows: In edge on projections of lamellar ($\alpha_2+\gamma$) colonies strain contrast is observed within α_2 lamellae that is not observed in binary γ -TiAl alloys, for example in [31]. In corresponding diffraction patterns taken in α_2 [10-10] orientation new reflections appear in addition to α_2 reflections indicating a reduction of the hexagonal symmetry in the orthorhombic phase. These are identified as reflections of the O-phase by comparison to simulated diffraction patterns, see [Figs. 2c, 3c](#). In α_2 or in the B19 phase no diffracted intensity appears at this

position. Dark field imaging with the -261 reflection unique to the O-phase (**Fig. 2b**) clearly demonstrates that the O-phase is located within α_2 lamellae, even though not the entire volume of the lath is occupied by O-phase (conclusion from HEXRD experiments in [24]). In high-resolution imaging in **Fig. 4** –also taken in α_2 [10-10] orientation– different contrast and diffraction behavior is observed in stripes perpendicular to the α_2/γ interface. The stripes extend across the entire width of the lamella– corresponding to the contrast modulations at lower magnification. Some of these stripes are identified as O-phase from analysis of image contrast and corresponding FFT (**Fig. 4b**, O-phase in [310] orientation). In adjacent regions the even brightness on all atom columns suggests presence of a disordered phase that is not unambiguously identified. Assuming that the effect of strain or tilt blurs the image contrast this could be any of the phases that matches the diffractogram in **Fig. 4c**– namely α_2 -[10-10], B19-[001] or O-phase-[010]. Bendersky et al. showed that the formation of O-phase proceeds directly from ordered α_2 phase while the B-19 phase forms during the transformation of β -phase to O-phase, figure 2 in [20]. In the same figure it can be seen that in principle the phase B19 may form via orthorhombically distorted, disordered α phase (A20). Therefore, no certain conclusion can be drawn on the nature of the 'disordered' stripes based on the presented high resolution images.

The strength of typical O-phase reflections in diffraction patterns in $\langle 1-100 \rangle$ orientation increases with annealing time at 550°C, which suggests that more α_2 phase transforms to O-phase during continued annealing. This is in agreement with HEXRD observations performed on the same specimen where the O-phase formation has been monitored in-situ [24].

Looking onto the α_2 hexagonal basal plane in α_2 [0001]-projection facets are seen inside α_2 lamellae. These have either rhomboid or rectangular shape and $\{1\bar{1}00\}$ and $\{1\bar{2}10\}$ type interfaces. The diffracted intensities in the corresponding diffraction patterns spread radially over a range of 3-5° around the position of hexagonal reflections suggesting that several small crystals contribute to the diffraction that are slightly rotated with respect to each other. At the same time, the spot splitting into two lattice-

spacings suggests that a new phase has formed. Considering the identification of O-phase in $\langle 1-100 \rangle$ diffraction patterns we conclude that the newly formed phase is the O-phase. The presence of the orthorhombic phase is likely to contribute to the radial distribution of diffracted intensities because the angles between reflections in the orthorhombic phase deviate from the 60° angle in the hexagonal structure. At higher magnification the distortion of $\alpha_2 \{10-10\}$ planes across the interface between differently ordered domains in **Fig. 8** illustrates that elastic strain acts within the microstructure. Similar observations of bent lattice planes and the presence of elastic stresses can be found in the reports by Muraleedharan et al. and Appel et. al. [32, 33]. Finally, a direct evidence for the orthorhombic lattice is shown in **Fig. 10** where displacement of atom positions along the three $\langle 1-100 \rangle$ directions of the (0001) basal plane destroys the hexagonal symmetry of the α_2 unit cell.

4.1 Geometry of α_2 /O-phase domains

Using the information obtained in edge-on and planar viewing directions it is possible to conclude on the morphology of the phases within the former α_2 lamellae. At low magnification the facets in [0001] viewing direction have rectangular or rhomboid shape defined by sets of $\{1-100\}$ and $\{11-20\}$ type interfaces (**Fig. 6**). Tilting the viewing direction by 90° to a $\langle 10-10 \rangle$ zone axis, well resolved stripes perpendicular to the $\alpha_2(0001)/\gamma_{\{111\}}$ interface are observed as illustrated in **Fig. 4**. Combining the information of both projections the following picture evolves: columns defined by $\{1-100\}$ and $\{11-20\}$ type interfaces populate the former 'pure' α_2 lath extending from one α_2/γ interface through the α_2 lamella to the opposite α_2/γ interface. These columns form by small atomic displacements in the (0001) plane along three $\alpha_2 \langle 11-20 \rangle$ directions as demonstrated in **Fig. 10**. As a result of these shifts, 3 different O-phase domains form - one corresponding to each displacement direction. Altogether, after annealing, the former α_2 laths consist of many small, columnar O-phase and α_2 crystallites that are slightly rotated with respect to each other. The strain between different domains is accommodated by

elastic bending of lattice planes, as seen in Fig. 8. The lattice strain complicates high-resolution imaging and is visible as strain contrast in edge-on projections (Fig. 2).

4.2 Comparison to literature on α_2 -based alloys with high Nb additions

The finding of O-phase in a γ -TiAl alloy with only 8.5 at.-% of Nb is new. We reported about it for the time using the results of in-situ heating synchrotron radiation [24]. Until now, in literature on γ -based alloys with comparable compositions only the orthorhombic phase B19 has been identified. The first reports on modulated microstructures in a γ -TiAl based alloy Ti-42-8.5Nb were published by Appel et al., who suggested that the orthorhombic phase B19 forms from ordered β_0 [10, 13, 33, 34]. Song et al. studied the alloy Ti-45Al-8.5Nb with trace amounts of W, B and Y and found that α_2 transforms to B19 during furnace cooling from 900 °C [12]. In both studies, the nature of the orthorhombic phase was determined from TEM observations in α_2 $\langle 11-20 \rangle$ direction which is not well suited to distinguish between the phases involved. Simulated diffraction patterns of the phases α_2 , B19 and O-phase are identical so that a distinction is obscured by superimposing reflections. For high-resolution imaging, simulated Bloch wave images show that the image contrast of the phases α_2 , B19 and O-phase is very similar when the presence of Nb is considered, preventing a clear distinction. Hence, it is well possible that in these alloys the O-phase is present instead of or in addition to the B19 phase. This could easily be checked by obtaining diffraction patterns in α_2 $\langle 1-100 \rangle$ direction. For comparison, in a binary alloy Ti-48Al the orthorhombic phase B19 was observed by high resolution imaging in α_2 [0001] direction where the two phases α_2 and B19 are clearly identified in image and in diffractograms [28].

In α_2 -based TiAl alloys with high Nb additions in the composition range Ti-(12-31)Al-(12.5-37)Nb the formation of O-phase has been observed repeatedly after annealing treatments. Banerjee was the first to observe a slightly distorted α_2 phase in Ti-25Al-12.5Nb by TEM that was identified as the ordered O-phase [14]. Later on; Muraleedharan et al. distinguished between an ordered O2-phase, where Nb takes

on specific lattice sites, and the disordered O1-phase, where Ti and Nb share the same lattice sites [19]. In the existing literature on α_2 -based alloys, globular α_2 or β_0 grains decompose into faceted arrangements like the ones we observe in the present alloy. [14, 16-22]. The facets are occupied by different variants of O-phase and remaining parent phase [20]. A major difference between our observations and earlier reports on the O-phase is that in our case the α_2 to O-phase transition takes place under the constraint condition in a lamellar ($\alpha_2 + \gamma$) colony- where the parent α_2 phase is sandwiched between γ lamellae.

Despite the spatially constraint situation in the lamellar ($\alpha_2 + \gamma$) colonies the similarities between the arrangement of domains is striking (see for instance Fig. 2c in [14]). Muraleedharan et al. studied the α_2 to O-phase transformation in Ti-28.5Al-13Nb during isothermal annealing at 900 °C [32]. The alloy's composition is richer in Ti and Nb which might explain the relatively high temperature of 900 °C at which the O-phase forms. The authors reported that O-phase domains form in α_2 grains in the shape of plates oriented perpendicular to the hexagonal α_2 (0001) plane, similar to our findings [32].

4.3 Position of Nb within microstructure

To our knowledge the formation of O-phase has been observed only in alloys with Nb addition and not in binary TiAl aluminides. Therefore an underlying question regarding the formation of O-phase is that about the role of Nb. Is the formation of O-phase preceded by the concentration of Nb in regions of the crystal that then undergo the transformation as suggested in [14]? Or does the transformation only involve short range ordering without change in composition over longer distances as reported in [18, 32]? We studied the composition of α_2 /O-phase lamellae by STEM-EDS and searched by EFTEM and HAADF for possible agglomerations of Nb. So far, no distinct lattice site for Nb was detected by these means, which might be explained by the low Nb content. In the HAADF image in Fig 10 some atom columns appear brighter than the neighboring ones, but these are distributed randomly throughout the

image. The lack of Nb clusters and the relatively short formation time during anneal (for example 2 h at 650 °C) suggest that the O-phase forms by small shifts of atomic positions over short distances without prior elemental ordering. This is in agreement with the finding in [18] that the O-phase may accommodate a variety of substitutional disorder and that ordering of Nb is not the specific driving force for the orthorhombic distortion.

4.4 In-situ heating

Regarding the range of chemical composition where the O-phase is stable, interesting in-sight can be gained from the results of the in-situ TEM heating experiment presented here. Our results show that during in-situ heating in the TEM the O-phase transforms back to α_2 phase at around 600 °C, and that the formed α_2 phase remains stable during subsequent cooling and repeated heating. These observations differ fundamentally from the results obtained by in-situ heating HEXRD experiments where the orthorhombic phase forms and dissolves reproducibly as the temperature is cycled around 700 °C [24].

In **Fig. 11** images and diffraction patterns of a TEM foil are shown at room temperature before the start of the heating experiment and after heating to 600 °C, e.g. after the $O \leftrightarrow \alpha_2$ transformation took place. In the edge-on projection in **Figs. 11 a, c** the strain contrast in the image and the O-phase reflections in the diffraction patterns are observed at room temperature but not after heating to 600 °C. Similarly, in the planar viewing direction facets are visible within α_2 laths at room temperature accompanied by spot splitting and spreading of diffracted intensities in the diffraction pattern in **Fig. 11b** but not after heating to 600 °C in **Fig. 11d**. These observations suggest that during heating the orthorhombic distortion is relaxed, i.e. the small atomic shifts parallel to α_2 - $\langle 11-20 \rangle$ directions in the hexagonal basal plane that initially formed the O-phase are reversed and the hexagonal symmetry is re-established throughout the entire α_2 lamellae. In-situ heating experiments at higher temperatures

have shown that oxidation of the foil sets in at temperatures above 740°C. The different experimental results obtained by in-situ heating experiments in the TEM and in the synchrotron can be explained looking at the dimensions of the investigated specimens. The HEXRD experiments were performed on cylindrical bulk specimens of 5 mm diameter and 10 mm length. Here, large volume fractions of the studied phases as well as large interface areas between lamellae and only an insignificant amount of surface area are present. For comparison, the illuminated area of the TEM foil measures $20 \times 20 \mu\text{m}^2$ with an estimated thickness in the range of $\leq 100\text{nm}$. This means that in the TEM foil large surface areas of either (α_2/O) or γ phase and negligible phase volume and interface area between α_2/O and γ lamellae are present. Considering, that the behavior of phases within the lamellar colonies depends on volume stresses and coherency stresses near the interfaces between the phases the thin TEM foil is not suited to represent the behavior of bulk material. During heating of the TEM foil the stress between (α_2/O) and γ lamellae can be relaxed and the transition from O-phase to α_2 phase takes place at a lower temperature than during the HEXRD experiments on bulk specimens. In the absence of the constraint posed by large interface areas between neighboring lamellae and the accompanying stress states, the α_2 phase remains stable during subsequent cooling – in contrast to the reversible $\text{O} \leftrightarrow \alpha_2$ transformation observed in bulk material during HEXRD heating experiments.

The influence of the specimen geometry on transformation of the O-phase suggests that the O-phase in the present alloy Ti-42Al-8.5Nb is stabilized by the presence of stresses in lamellar $\alpha_2 + \gamma$ colonies.

Regarding the interpretation of the experimental electron diffraction patterns, the in-situ observations confirm that the observed electron diffraction patterns of the O-phase originate from an orthorhombic crystal and not from the presence of Nb on lattice sites of a hexagonal lattice.

5. CONCLUSIONS

In the alloy Ti-42Al-8.5Nb, the orthorhombic O-phase was identified by single electron diffraction and high-resolution imaging. The chemical composition of α_2 lamellae was Ti-37Al-9Nb and no Nb enriched regions were detected before or after annealing at 650 °C and 550 °C. The transition from the hexagonal α_2 phase to the orthorhombic lattice takes place by the displacement of atom columns along $\langle 11\text{-}20 \rangle$ directions of the hexagonal lattice and was directly imaged by HAADF. The O-phase domains and domains of residual α_2 phase have the shape of columnar crystallites that occupy the volume of the compound α_2 /O-phase laths. The crystallites extend along the α_2 [0001] direction across the former α_2 lamellae and are defined by {1-100} and {11-20} interfaces. Elastic strain between different domains is visible in form of bent lattice planes in high-resolution [0001] projections and in the form of strain contrast at lower magnification in $\langle 1\text{-}100 \rangle$ edge-on projections of lamellar colonies. In the absence of volume and coherency stresses that act within lamellar (α_2 /O + γ) colonies the O-phase irreversibly transforms back to α_2 during heating to about 600 °C which suggests that the stress states within lamellar colonies play a role in the phase stability.

ACKNOWLEDGEMENTS

The authors thank Chris Boothroyd and the Ernst Ruska-Centre (ER-C) for Microscopy and Spectroscopy with Electrons for realization of the EFTEM experiments and Anna Carlsson of FEI for helpful discussions on the evaluation of EDS spectra with the program TIA.

6. REFERENCES

- [1] Y.-W. Kim, Effects of microstructure on the deformation and fracture of γ -TiAl alloys, *Materials Science & Engineering A* 192/193 (1995) 519-533.
- [2] D.M. Dimiduk, Gamma titanium aluminide alloys- an assessment within the competition of aerospace structural materials, *Materials Science and Engineering A* 263 (1999) 281-288.
- [3] X. Wu, Review of alloy and process development of TiAl alloys, *Intermetallics* 14 (2006) 1114-1122.
- [4] G. Electric, <http://www.flightglobal.com/news/articles/power-house-207148/> (2012).
- [5] C. McCullough, J.J. Valencia, C.G. Levi, R. Mehrabian, Phase Equilibria and Solidification in TiAl Alloys, *Acta metall.* 37(5) (1989) 1321-1336.
- [6] F. Appel, M. Oehring, R. Wagner, Novel design concepts for gamma-base titanium aluminide alloys, *Intermetallics* 8 (2000) 1283-1312.
- [7] Z.C. Liu, J.P. Lin, S.J. Li, G.L. Chen, Effects of Nb and Al on the microstructures and mechanical properties of high Nb containing TiAl base alloys, *Intermetallics* 10(7) (2002) 653-659.
- [8] W.J. Zhang, F. Appel, Effect of Al content and Nb addition on the strength and fault energy of TiAl alloys, *Materials Science and Engineering A* 329-331 (2002) 649- 652.
- [9] F. Appel, J. Paul, M. Oehring, *Gamma Titanium Aluminide Alloys*, Wiley-VCH Verlag GmbH & Co. KGaA2011.
- [10] F. Appel, M. Oehring, J.D.H. Paul, Nano-scale Design of TiAl Alloys Based on β -Phase Decomposition, *Advanced Engineering Materials* 8(5) (2006) 371-376.

- [11] H. Jabbar, J.-P. Monchoux, F. Houdellier, M. Dollé, F.-P. Schimansky, F. Pyczak, M. Thomas, A. Couret, Microstructure and mechanical properties of high niobium containing TiAl alloys elaborated by spark plasma sintering *Intermetallics* 18 (2010) 2312- 2321.
- [12] L. Song, X.J. Xu, L. You, Y.F. Liang, J.P. Lin, B19 phase in Ti-45Al8.5Nb-0.2W-0.2B-0.02Y alloy, *Journal of Alloys and Compounds* 618 (2015) 305-310.
- [13] F. Appel, M. Oehring, J.D.H. Paul, A novel in situ composite structure in TiAl alloys, *Materials Science and Engineering A-Structural Materials Properties Microstructure and Processing* 493(1-2) (2008) 232-236.
- [14] D. Banerjee, A.K. Gogia, T.K. Nandi, V.A. Joshi, A new ordered orthorhombic phase in a Ti_3Al-Nb alloy *Acta metall.* 36(4) (1988) 871-882.
- [15] F. Chu, T.E. Mitchell, B. Majumdar, D. Miracle, T.K. Nandy, D. Banerjee, Elastic Properties of the O-phase in Ti-Al-Nb alloys *Intermetallics* 5 (1997) 147- 156.
- [16] L.A. Bendersky, W.J. Boettinger, A. Roytburd, Coherent Precipitates in the bcc/ orthorhombic two-phase field of the Ti-Al-Nb System *Acta metall. mater.* 39(8) (1991) 1959-1969.
- [17] K. Muraleedharan, A.K. Gogia, T.K. Nandy, D. Banerjee, S. Lele, Transformations in a Ti-24-Al-15Nb Alloy : Part I. Phase Equilibria and Microstructure, *Metallurgical Transactions A* 23A (1992) 401-415.
- [18] K. Muraleedharan, T.K. Nandy, D. Banerjee, S. Lele, Transformations in a Ti-24Al-15Nb alloy: part II. A Composition Invariant $\beta_o \rightarrow O$ Transformation, *Metallurgical and Materials Transactions A* 23A(February) (1992) 417-431.
- [19] K. Muraleedharan, T.K. Nandy, D. Banerjee, S. Lele, Phase stability and ordering behavior of the O phase in Ti-Al-Nb alloys *Intermetallics* 3 (1995) 187-199.
- [20] L.A. Bendersky, A. Roytburd, W.J. Boettinger, Phase Transformations in the (Ti, Al)₃Nb Section of the Ti-Al-Nb-System-I. Microstructural Predictions based on a Subgroup Relation between Phases, *Acta metall. mater.* 42(7) (1994) 2323-2335.

- [21] L.A. Bendersky, W.J. Boettinger, Phase Transformations in the (Ti, Nb)₃Al Section of the Ti-Al-Nb-System-II. Experimental TEM Study of Microstructures, *Acta metall. mater.* 42(7) (1994) 2337-2352.
- [22] Y.H. Wen, Y. Wang, L.A. Bendersky, L.Q. Chen, Microstructural evolution during the $\alpha_2 \rightarrow \alpha_2 + O$ transformation in Ti-Al-Nb alloys : phase-field simulation and experimental validation, *Acta mater.* 48 (2000) 4125-4135.
- [23] J. Kumpfert, Intermetallic Alloys Based on Orthorhombic Titanium Aluminides, *Advanced Engineering Materials* 3(11) (2001) 851-864.
- [24] M.W. Rackel, A. Stark, H. Gabrisch, N. Schell, A. Schreyer, F. Pyczak, Orthorhombic phase formation in a Nb-rich γ -TiAl based alloy – an in situ synchrotron radiation investigation, *Acta Materialia* 121 (2016) 343-351.
- [25] R. Gerling, H. Clemens, F.P. Schimansky, Powder Metallurgical Processing of Intermetallic Gamma Titanium Aluminides, *Advanced Engineering Materials* 6(1-2) (2004) 23-38.
- [26] J. Barthel, L. Houben, K. Tillmann, FEI Titan G3 50-300 PICO, *Journal of large-scale research facilities* JLSRF A 34 (2015) 1-4.
- [27] D.G. Konitzer, I.P. Jones, H.L. Fraser, Site Occupancy in Solid Solutions of Nb in the Intermetallic Compounds TiAl and Ti₃Al *Scripta Metallurgica* 20 (1986) 265-268.
- [28] E. Abe, T. Kumagai, M. Nakamura, New ordered structure of TiAl studied by high-resolution electron microscopy, *Intermetallics* 4(4) (1996) 327-333.
- [29] H. Gabrisch, U. Lorenz, M. Oehring, J. Paul, F. Pyczak, M. Rackel, F.-P. Schimansky, A. Stark, TiAlNb-alloy with a modulated B19 containing constituent produced by powder metallurgy, *MRS Proceedings (Symp. JJ) (2012 MRS Fall Meeting)*.
- [30] M.J. Blackburn, SOME ASPECTS OF PHASE TRANSFORMATIONS IN TITANIUM ALLOYS, *Science, Technology, and Application of Titanium* (1970) 633-643.

- [31] M. Oehring, F. Appel, P.J. Ennis, R. Wagner, A TEM study of deformation processes and microstructural changes during long-term tension creep of a two-phase γ -titanium aluminide alloy, *Intermetallics* 7 (1999) 335-345.
- [32] K. Muraleedharan, D. Banerjee, The α_2 -to-O-phase transformation in Ti-Al-Nb alloys *Philosophical Magazine A* 71(5) (1995) 1011-1036.
- [33] F. Appel, J.D.H. Paul, M. Oehring, Phase transformations during creep of a multiphase TiAl-based alloy with a modulated microstructure, *Materials Science and Engineering a-Structural Materials Properties Microstructure and Processing* 510-11 (2009) 342-349.
- [34] F. Appel, M. Oehring, J.D.H. Paul, Physical metallurgy and performance of the TNB and γ -md alloys, in: W.S. Young-Won Kim, Junpin Lin, Dennis Dimiduk, and Fritz Appel (Ed.) *TMS 2014 - 143rd Annual Meeting & Exhibition of the Minerals, Metals, and Materials San Diego, CA, USA, 2014*.

APPENDIX

Unit cells

α_2 -phase composition Ti-40Al-10Nb, space group 194, P $6_3/m m c$, a=0.5775 nm , c=0.4638 nm

Wyck.	x	y	z	Element	at.-%	occ.
2d	1/3	2/3	3/4	Al	25	1.00
6h	1/6	1/3	1/4	Al	15	0.20
6h	1/6	1/3	1/4	Ti	50	0.67
6h	1/6	1/3	1/4	Nb	10	0.13

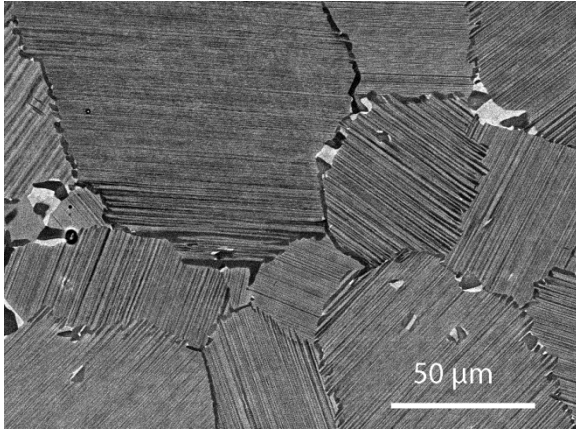
B19-phase composition Ti-40Al-10Nb, space group 51, P m m a, a=0.465 nm ,b=0.290 nm ,
c=0.490 nm

Wyck.	x	y	z	Element	at.-%	occ.
2e	1/4	0	1/3	Ti	50	1.0
2f	1/4	1/2	5/6	Al	40	0.8
2f	1/4	1/2	5/6	Nb	10	0.2

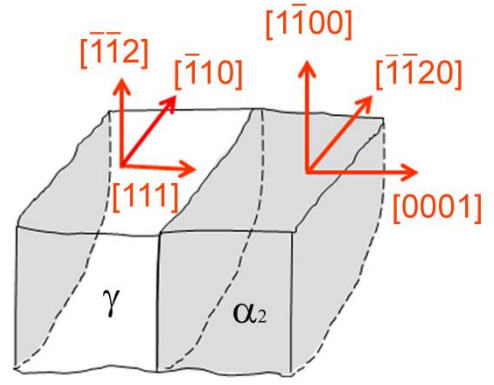
O-phase- composition Ti-40Al-10Nb, space group 63, C m c m, a=0.610 nm,b=0.957 nm , c=0.462 nm

Wyck.	x	y	z	Element	at.-%	occ.
8g	0.231	0.904	1/4	Ti	50	1.0
4c1	0	0.163	1/4	Al	25	1.0

4c2	0	0.636	1/4	Al	15	0.6
4c2	0	0.636	1/4	Nb	10	0.4



a.)



b.)

Figure 1: SEM Image and schematic representation of lamellar ($\alpha_2 + \gamma$) colonies.

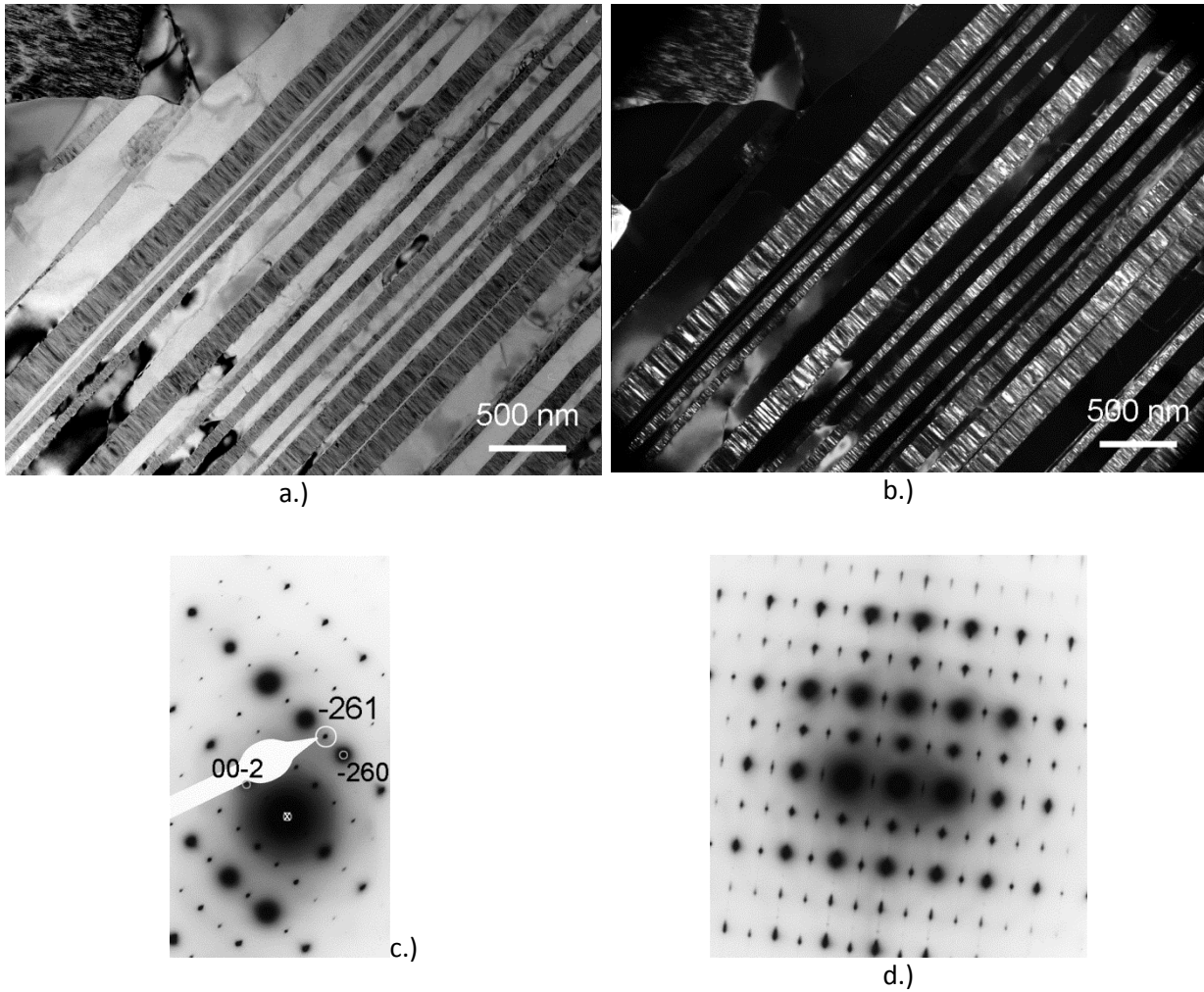


Figure 2:

- a.) Bright field image of lamellar colony in α_2 -[10-10] orientation. The α_2 /O-phase laths appear in dark image contrast, γ -lamellae appear in bright contrast.
- b.) Dark field image of the same specimen region recorded with the -261 reflection of the O-phase.
- c.) Diffraction pattern illustrating the dark-field imaging condition (O-phase-[310], -261).
- d.) Diffraction pattern in α_2 -[10-10] orientation parallel to O-phase [310] taken of a specimen annealed at 550°C for 504 h (3 weeks).

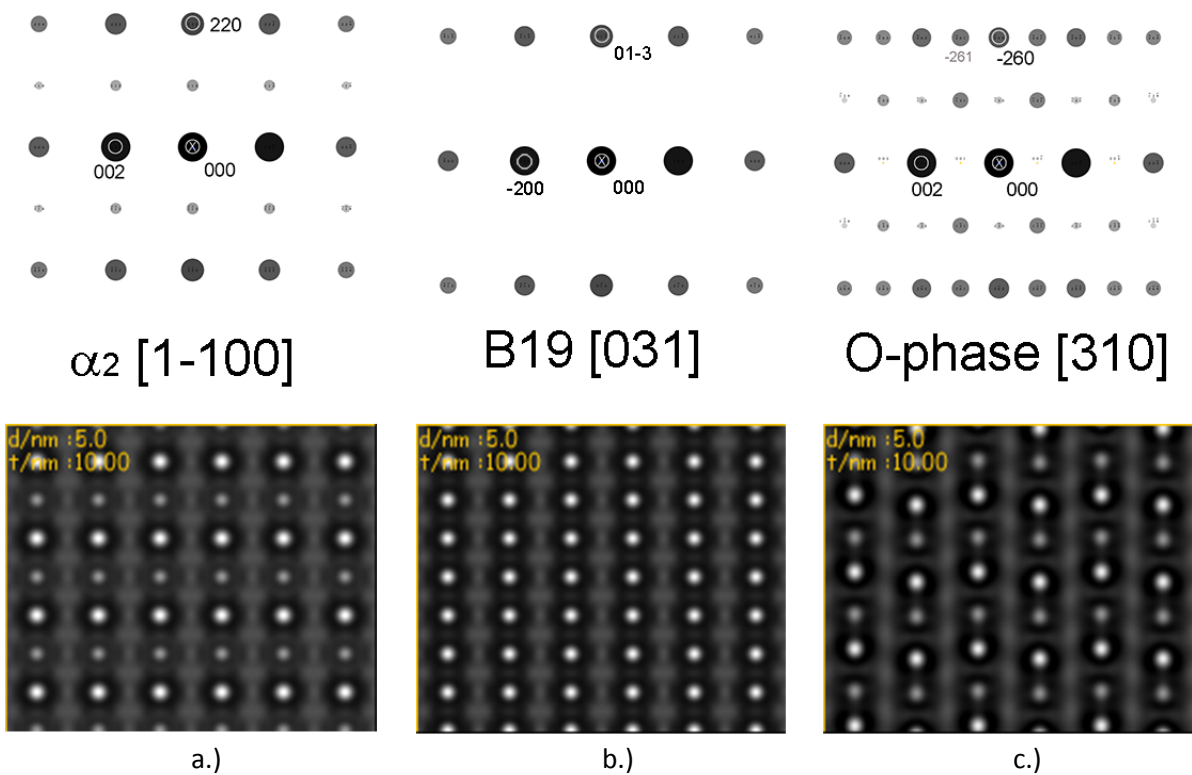


Figure 3: a. Simulated electron diffraction pattern and Bloch wave image of α_2 in [10-10] orientation. b.) and c.) show the corresponding diffraction patterns and Bloch wave images for the B19 and O-phase in the directions B19-[031] and O-phase-[310]. The images were calculated for a thickness of 10nm at 5 nm defocus and $C_s = 0.01$ mm. Image and diffraction of B-19-[001] and O-phase-[010] are identical to those of α_2 in [10-10] (see additional material).

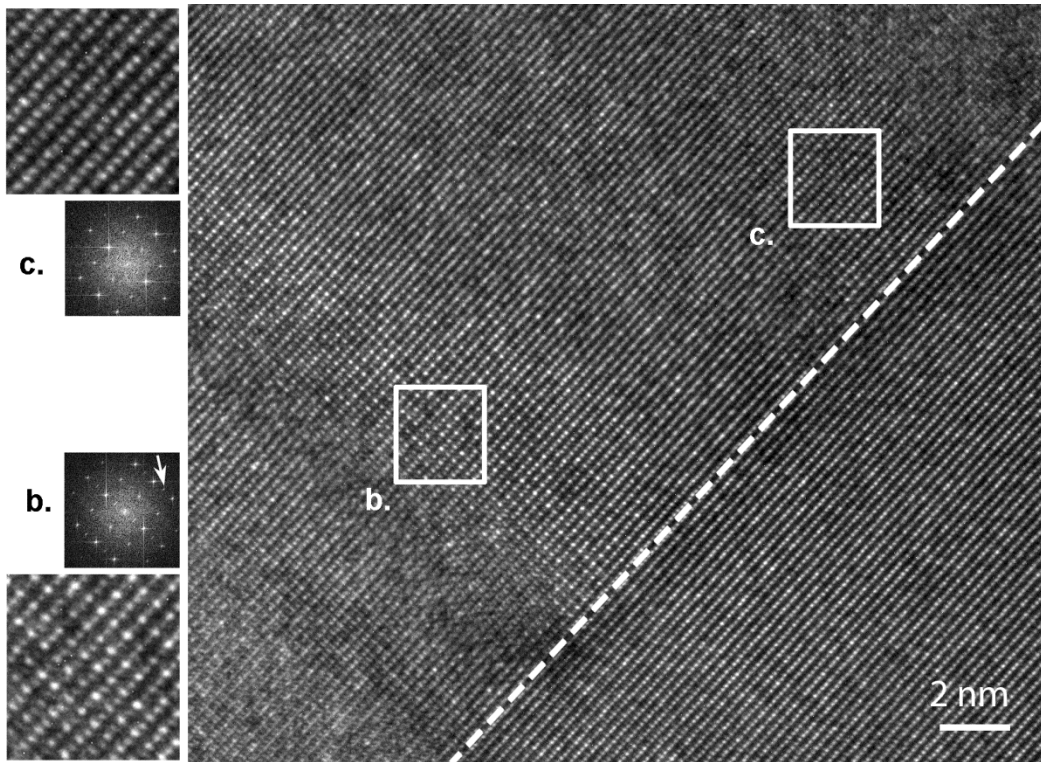


Figure 4 : High-resolution image in α_2 -[10-10] orientation showing part of an α_2 /O-phase lath (left) and neighboring γ phase (right), defocus 5nm. The position of the interface is marked by the broken line.
b.), c.) Magnification of regions b. and c. together with corresponding Fast Fourier Transformation (FFT). In the FFT of b. one of the O-phase reflections is marked by a small arrow.

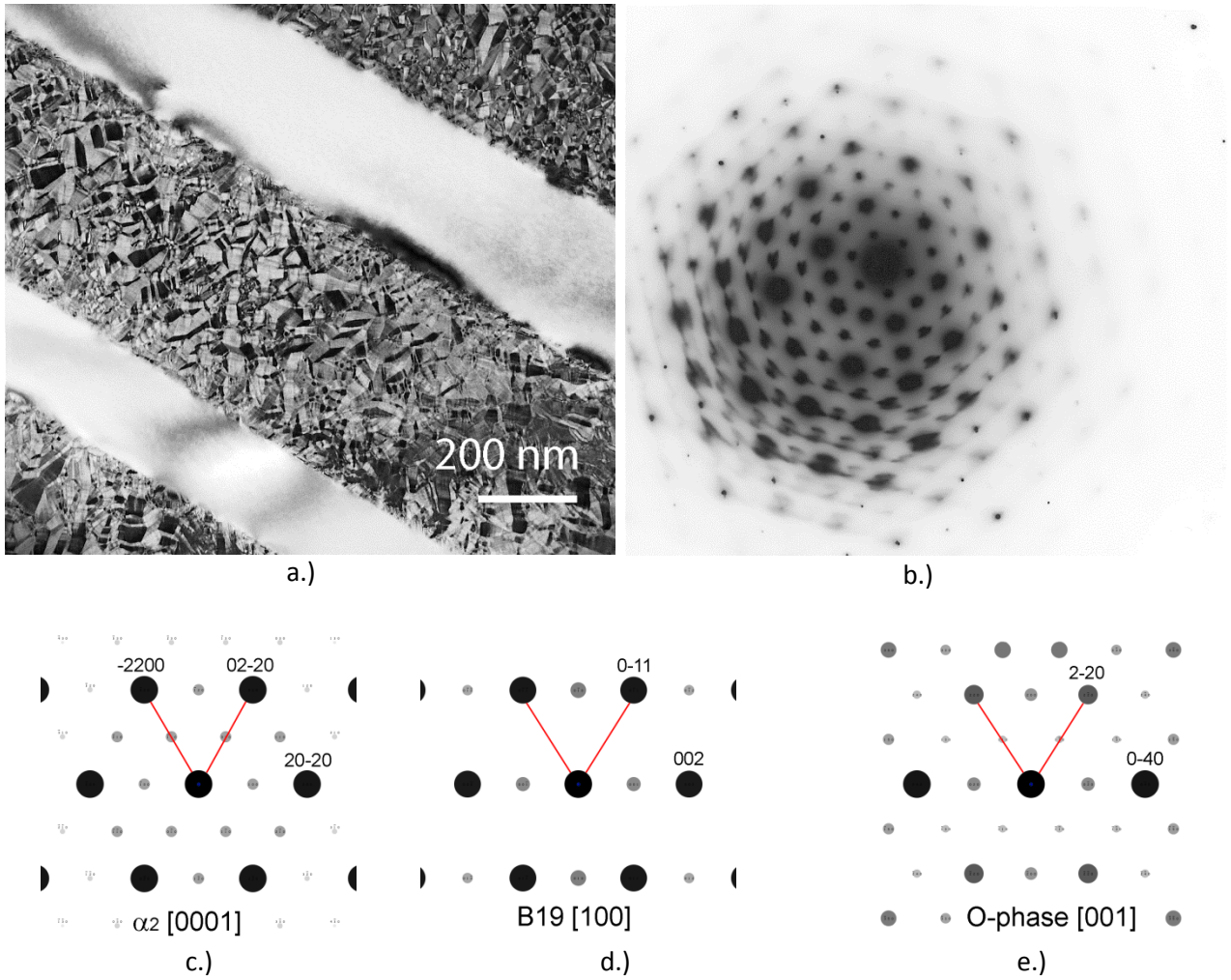


Figure 5 Planar view of a transformed lamellar ($\alpha_2 + \gamma$) colony. a.), b.) Bright field image of an α_2 /O-phase lamella in α_2 -[0001] orientation and corresponding diffraction pattern. c.)-d.) Simulated diffraction patterns of α_2 in [0001]-orientation, of B19 in [100] orientation and of O-phase in [001] orientation.

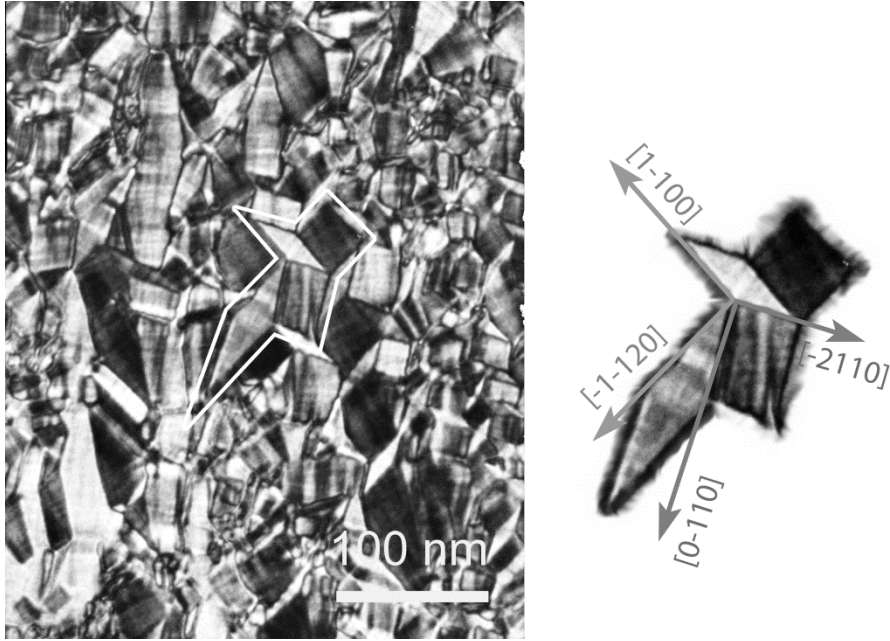
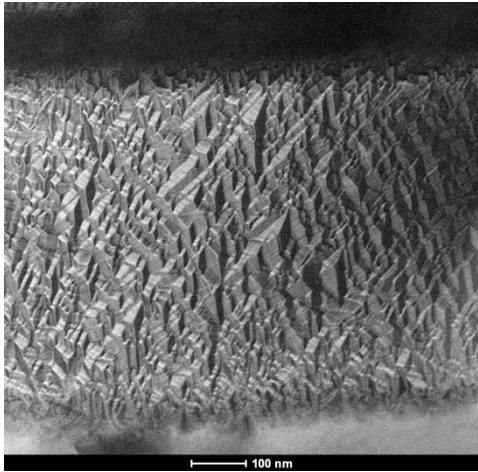
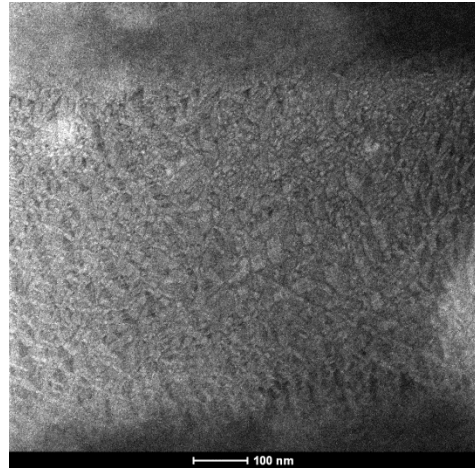


Fig. 6 : Section of α_2 /O-phase lamella. The enlarged section on the right illustrates the orientation of interfaces that define rectangular and rhomboid facets.



a.)



b.)

Figure 7 : HAADF-STEM images of α_2 O-phase lamella in [0001] orientation recorded with camera length $L=300\text{m}$ (predominantly diffraction contrast, a.) and camera length $L= 100\text{mm}$ (predominantly z-contrast, b.).

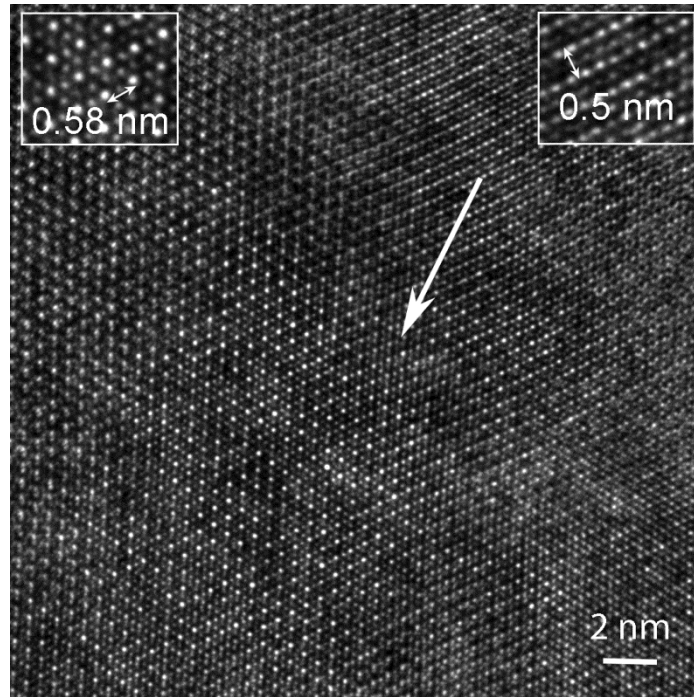


Figure 8 : High resolution image of α_2 /O-phase lath in [0001] orientation. Atomic ordering of six-fold and two-fold symmetry is observed in neighboring regions (defocus: 25 nm).

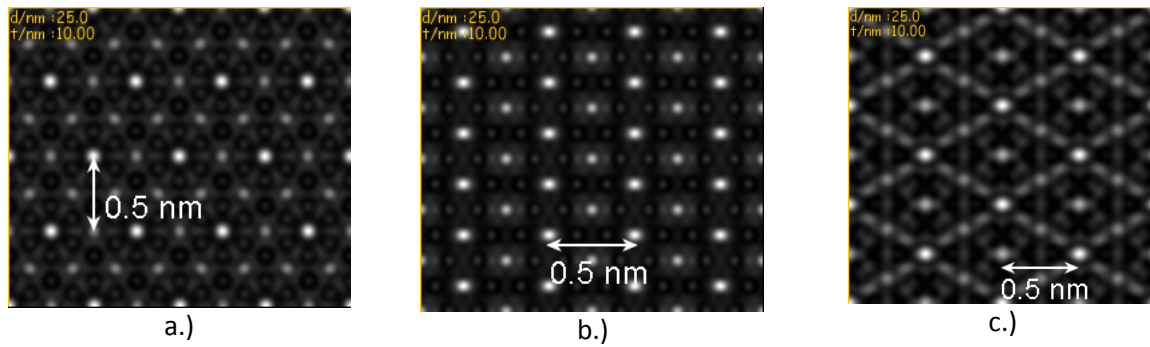


Figure 9: Simulated Bloch wave images for the phases α_2 (a.), B19 (b.) and O phase (c.) parallel to the α_2 [0001] zone axis. The images are calculated for a specimen thickness of 10nm, defocus value 25 nm and $C_s = 0.01\text{mm}$. Tables for images obtained under variation of thickness and defocus are provided as additional material.

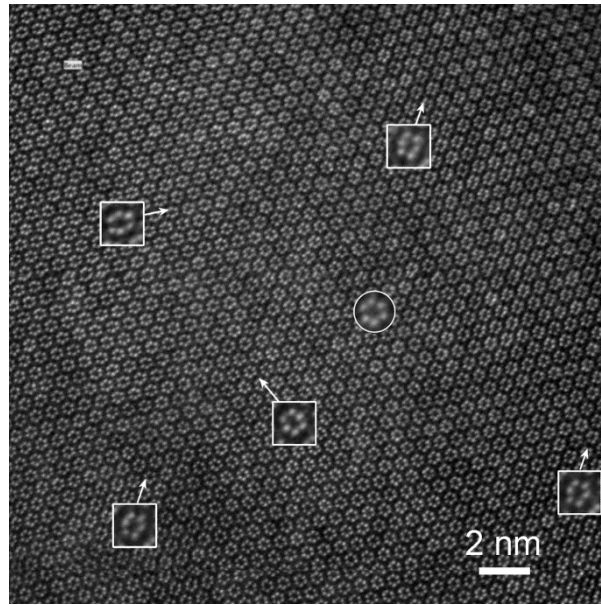


Figure 10 : a.) HAADF image illustrating the orthorhombic distortion of the lattice along the three $\langle 11\text{-}20 \rangle$ directions of the hexagonal lattice in the parent α_2 phase. The direction of the distortion is indicated by arrows attached to enlarged sections of the image.

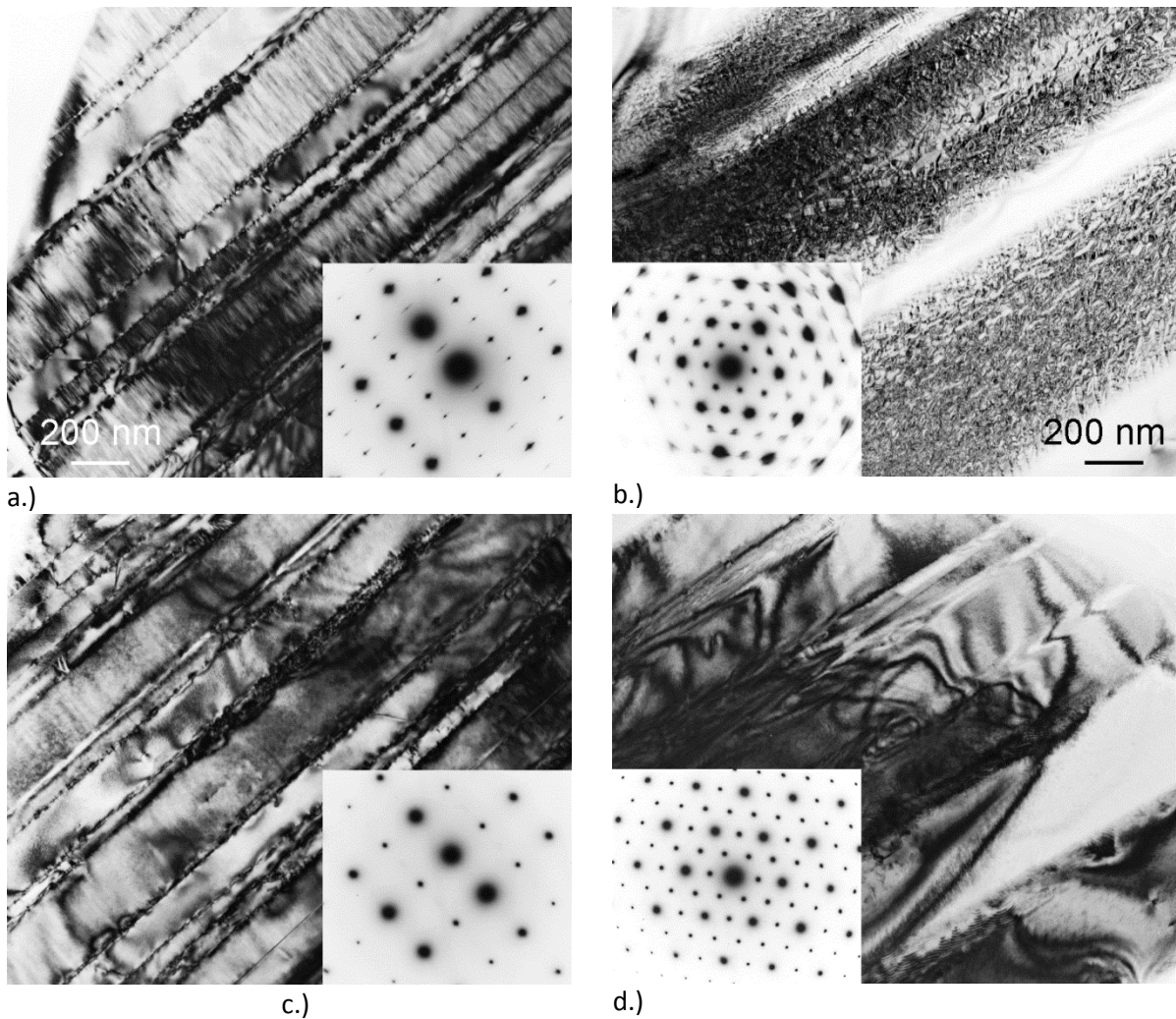


Figure 11: Reversal of orthorhombic distortion during in-situ heating of thin TEM foil.

a.), b.) Taken at room temperature, before the heating experiment: Strain contrast in edge on viewing direction (a.) is accompanied by faceting in planar view (b.). Typical O-phase reflections and steaking of diffraction spots are observed in the edge-on $[10-10]$ zone axis direction. The diffraction pattern in $[0001]$ direction shows spot splitting and spreading of intensities that indicate presence of multiple phases and many small crystallites.

c., d.) Recorded at room temperature after heating to 600°C . The strain contrast and the faceting observed before heating are removed. In the $[10-10]$ zone axis direction diffraction pattern in c.) the typical O-phase reflections are no longer observed. In the $[0001]$ diffraction pattern in d.) no signs of multiple phases are detected.